

1 Retention of  $^{226}\text{Ra}$  by barite:  
2 the role of internal porosity

3 *Juliane Weber<sup>1\*</sup>♦, Juri Barthel<sup>2,3</sup>, Martina Klinkenberg<sup>1</sup>, Dirk Bosbach<sup>1</sup>, Maximilian Kruth<sup>2,3</sup>,*  
4 *Felix Brandt<sup>1</sup>*

5 <sup>1</sup>Institute of Energy and Climate Research (IEK-6) – Nuclear Waste Management and  
6 Reactor Safety, Forschungszentrum Jülich GmbH, 52425 Jülich, Germany

7 <sup>2</sup>Central Facility for Electron Microscopy (GFE), RWTH Aachen, Germany

8 <sup>3</sup>Ernst Ruska-Centre for Microscopy and Spectroscopy with Electrons (ER-C),  
9 Forschungszentrum Jülich GmbH, 52425 Jülich, Germany

10  
11 **Abstract**

12 The role of internal macropores and nano-scale pores for the uptake of  $^{226}\text{Ra}$  into barite was  
13 studied via scanning and transmission electron microscopy as well as focused ion beam  
14 methods. A temporal evolution of the internal microstructure and the Ra distribution was  
15 observed on samples taken from long-term Ra uptake experiments. The results of this study  
16 clearly show a significant impact of the presence of Ra leading to a complete reconstruction  
17 of the internal barite microstructure, whereas the microstructure of Ra-free reference samples  
18 remained unchanged. The initial internal barite microstructure contains a connected network

19 of macropores and a layered structure of nano-scale pores which, in the presence of Ra,  
20 coalesced in favor of larger pores during the experiment. A clear relationship between the Ra  
21 uptake and the internal porosity was observed by high-resolution STEM-EDX mappings.  
22 Starting from strongly enhanced Ra concentrations in the solid in the vicinity of the pores, Ra  
23 is temporarily inhomogeneously distributed within the barite particles. At later stages of the  
24 long-term experiment the Ra distribution becomes homogenous while nano-scale and macro-  
25 scale pores disappear. In conclusion, the uptake of Ra into barite takes place by a special case  
26 of dissolution/reprecipitation from the inside of the particle to the outside.

27

28 **Keywords:** Radium, barite, solid solution formation, dissolution/reprecipitation, nuclear  
29 waste management, electron microscopy, elemental mapping, FIB-SEM tomography

30

## 31 **1. Introduction**

32 The long-term fate of  $^{226}\text{Ra}$  is of great environmental relevance due to its ubiquitous  
33 occurrence in the oil, gas and coal exploration and extraction and the resulting naturally  
34 occurring radioactive materials (NORM) (Varley et al., 2016; Attalah et al., 2015; Kondash et  
35 al., 2014; Rosenberg et al., 2014). Ra is one of the most important primary sources of  
36 elevated radioactivity created by industrial activity, energy production and mining. Co-  
37 precipitation and solid solution formation of Ra-phases with sparingly soluble sulfates,  
38 especially barite, leads to unwanted radioactive scale formation (Kondash et al., 2014; Al  
39 Attar et al., 2016).

40 Recently, the role of solid solution formation as an essential process for the remediation of  
41 contaminants was discussed (e.g. review of Prieto et al., 2016). In the case of Ra, the same  
42 mechanism which leads to unwanted radioactive scales is also applied to reduce the levels of  
43 Ra in the environment to legal standards, e.g. for the NORM removal from hydraulic

44 fracturing fluids. Therefore, the formation of the (Ba,Ra)SO<sub>4</sub> solid solution from high  
45 supersaturation has been intensively studied with respect to technical processes for the Ra  
46 removal (e.g. Stoica et al., 1998; Chalupnik et al., 2008). A recent review on the treatment of  
47 water contaminated with Ra poses the question of the long-term stability of the (Ba,Ra)SO<sub>4</sub>  
48 when disposed in lakes (IAEA, 2014). This open question still seems to hinder the application  
49 of (Ba,Ra)SO<sub>4</sub> co-precipitation for processing contaminated water.

50 Ra uptake at close-to-equilibrium conditions refers to the long-term behavior of Ra in the  
51 environment (Zhang et al., 2014; Rosenberg et al., 2011a, b). The special case of the contact  
52 between pre-existing barite and Ra in solution and their possible re-equilibration to a  
53 (Ba,Ra)SO<sub>4</sub> solid solution at close-to-equilibrium conditions has been a question of interest in  
54 several recent publications (e.g. Grandia et al., 2008; Bruno et al., 2007; Curti et al., 2010;  
55 Brandt et al., 2015; Torapava et al., 2014), because <sup>226</sup>Ra is a key radionuclide in safety  
56 assessments of deep geological waste repositories for spent nuclear fuel. (Ba,Ra)SO<sub>4</sub> was  
57 recognized as possibly solubility limiting phase for Ra in the context of direct disposal of  
58 spent nuclear fuel. Based on thermodynamic considerations, uptake into pre-existing barite is  
59 predicted to be the main scavenger of Ra in several scenarios (Vinograd et al., 2013).

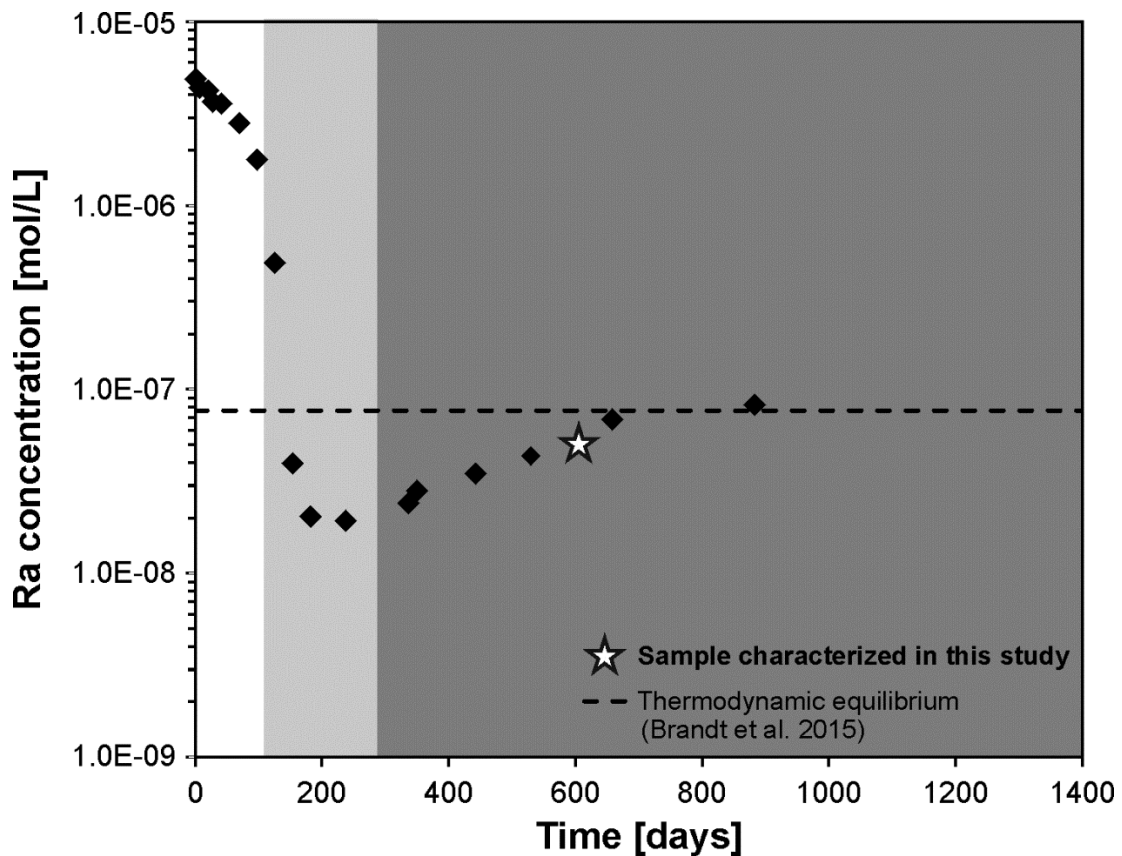
60 Recent experimental results demonstrated a complete recrystallization of pre-existing barite  
61 in the presence of Ra in time-scales of several hundred days (Bosbach et al., 2010; Curti et  
62 al., 2010). A detailed experimental study presenting repetitive long-term batch-  
63 recrystallization experiments was carried out by Brandt et al. (2015). This study provides an  
64 in-depth analysis of the solution chemistry, modelling of kinetics and thermodynamic data of  
65 the Ra uptake into barite based on a number of experiments conducted under carefully  
66 selected experimental parameters (solid/liquid ratio, grain size, and specific surface area).

67 A general trend of the temporal evolution of the Ra concentration in solution in such  
68 experiments is discussed in Brandt et al. (2015) and can be summarized by the following

69 three stages describing three different kinetic regions (Fig. 1), (1) slow initial decrease of the  
70 Ra concentration; (2) a faster decrease to a minimum Ra concentration below the predicted  
71 thermodynamic equilibrium (dashed line in Fig. 1) and (3) approach to thermodynamic  
72 equilibrium. The Ra-concentration in the solution is decreased by about 99.99 % of its initial  
73 value (Brandt et al., 2015).

74

75 Due to different onset times of the fast Ra decrease in solution, the concentration plateau  
76 was reached during a time interval of 600 to 1100 days (Brandt et al., 2015).



77

78 Fig. 1. Temporal evolution of the aqueous Ra concentration during a Ra uptake experiment as  
79 discussed by Brandt et al. (2015). The white area refers to stage 1, the light grey area to stage 2 and  
80 the dark grey area to stage 3 of the Ra-uptake. A sample from this experiment (★) was taken for  
81 comparison with an experiment carried out in the present study.

82

83 In order to gain fundamental insights into the uptake process, microscopic studies were  
84 conducted analyzing the barite morphology before and after the Ra uptake in comparison to  
85 Ra-free reference experiments (Klinkenberg et al., 2014). In this previous work, only very  
86 little changes of the outer shape and size of the barite particles were observed, leading to the  
87 conclusion that the uptake of Ra must be related to internal processes. The spatial resolution  
88 of the ToF-SIMS analysis provided in the same study allowed for the distinction between a  
89 surface layer and the Ra uptake into the crystal volume (Klinkenberg et al., 2014). Ra was  
90 clearly identified within the barite crystal volume. However, the pathways enabling the Ra  
91 uptake into barite and the temporal evolution of the Ra distribution within the newly formed  
92 solid-solution remained unclear. The studies of Brandt et al. (2015) and Klinkenberg et al.  
93 (2014) are forming the basis for the here presented results. As the study of Brandt et al.  
94 (2015) provides the complete and detailed description of the evolution of the Ra-  
95 concentration, the solution chemistry is only briefly covered here.

96 At ambient conditions, a replacement of pure barite by (Ba,Ra)SO<sub>4</sub> via solid state diffusion  
97 starting from the particle surface would be too slow for a complete exchange considering  
98 diffusion rates in minerals depicted e.g. in Zhang et al. (2008 and 2010). An alternative  
99 mechanism could be dissolution-reprecipitation, which has been recently studied extensively  
100 (e.g. reviews of Ruiz-Agudo et al., 2014; Altree-Williams et al., 2015). Despite the wide  
101 recognition of internal mineral phase exchange due to pseudomorphic replacement (e.g. Ruiz-  
102 Agudo et al., 2014; Altree-Williams et al., 2016; Putnis & Putnis, 2007; Hellmann et al.,  
103 2015), the underlying mechanisms remains not fully understood. The current understanding is  
104 that during a dissolution-reprecipitation process, a mineral phase AC consisting of a cation A  
105 and an anion C re-equilibrates due to a disequilibrium with another cation B in solution. This  
106 leads to the subsequent precipitation of the less soluble solid solution (A,B)C. For a complete

107 exchange, the interface between the solid and the aqueous solution needs to stay connected to  
108 the bulk fluid. Therefore, the newly precipitated phase needs to be porous.

109 The replacement of a parent mineral phase by a product phase is accompanied by changes  
110 in the overall porosity. Two main factors have an effect on this change in porosity. The first  
111 factor is the difference in the molar volume between the parent and the product phase. In  
112 addition, the second factor influencing the change in porosity is the solubility of the two  
113 phases (Putnis & Austrheim, 2013; Ruiz-Agudo et al., 2014). The solubility is determined by  
114 the grain size, fluid composition, temperature and pressure among other factors and will  
115 change during the replacement process. Large differences in solubility between parent phase  
116 (more soluble) and product phase (less soluble) might results in parent material loss during  
117 the reaction leading to an increased pore space in the product phase. Also, an increase in  
118 molar volume during replacement from the parent phase to the product phase can still result  
119 in a higher porosity. This was observed e.g. for the replacement of leucite by analcime  
120 (Putnis et al., 2007) or magnetite by pyrite (Qian et al., 2010). Furthermore, the strain which  
121 is related to high volume change reaction can induce fracturing which provides new pathways  
122 for fluid infiltration.

123 The change in porosity was defined by Pollock et al. (2011) not only regarding the molar  
124 volume but also the relative solubilities (Eq. 1):

$$V = 100 \times \left( \frac{n_p V_{m,p} - n_d V_{m,d}}{n_d V_{m,d}} \right) \quad (1)$$

125 Where  $n_d$  and  $n_p$  are the number of moles of the parent dissolved and the product  
126 precipitated and  $V_{m,d}$  and  $V_{m,p}$  are the molar volumes of the dissolving and precipitating  
127 phase respectively. For further references Altree-Williams et al. (2015) provide an extensive  
128 review on textural changes during mineral replacement by dissolution and reprecipitation.

129 The change in molar volume for the exchange of barite by a  $Ba_xRa_{1-x}SO_4$  solid solution can

130 be estimated considering the change in molar volume by a complete replacement of barite by  
131 pure RaSO<sub>4</sub> first. Using equation (1), the change in molar volume can be calculated using the  
132 molar volumes of barite (47.95 cm<sup>3</sup>/mol) based on Hanor (2000) and a molar volume of pure  
133 RaSO<sub>4</sub> of 55.87 cm<sup>3</sup>/mol (Weigel & Trinkl, 1968). The precipitated and dissolved moles are  
134 set to one assuming complete replacement.

$$\Delta V = \left( \frac{1 \times 55.87 - 1 \times 47.95}{1 \times 55.87} \right) = 14.17 \% \quad (2)$$

135 Accordingly, the change in molar volume for the complete replacement of barite by pure  
136 RaSO<sub>4</sub> would be 14.17 %.

137 The solubility of barite is well studied over a range of temperatures and for this calculation,  
138 the solubility at ambient conditions provided by Blount (1977) of logK<sub>BaSO<sub>4</sub></sub> of -9.97 is used.  
139 For RaSO<sub>4</sub>, the solubility constant implemented in the Nagra-PSI database (Thoenen et al.,  
140 2014) is logK<sub>RaSO<sub>4</sub></sub> = -10.26 as obtained by Langmuir and Riese (1985). Therefore, the  
141 difference in solubility between barite and RaSO<sub>4</sub> is less than 2.8 %.

142 A complete exchange of barite by radiobarite with a sufficient amount of Ra in solution  
143 would be expected to be accompanied by considerable microstructural changes. In contrast,  
144 the complete exchange with the relatively small amount of Ra provided in the experiments of  
145 Brandt et al. (2015) would be expected to lead only to minor microstructural changes.

146 The replacement process of mineral phase AC by a (A,B)C solid solution is based on the  
147 thermodynamic principle of energy minimization, yet this does not completely explain the  
148 kinetic driving forces. Only very little information is so far available about the kinetic driving  
149 forces controlling the mineral recrystallization and contaminant uptake relevant to the  
150 environment. Based on a detailed study of calcite, Ostwald ripening driven by surface energy  
151 minimization has been proposed as one important mechanism for recrystallization (Heberling  
152 et al., 2016). In a recent review about mineral recrystallization at low temperatures (<100 °C)

153 the importance of applying high resolution microscopy techniques has been emphasized to  
154 gain further insights into the molecular scale mechanism of stable mineral recrystallization  
155 (Gorski et al., 2016).

156 It is well known that natural barites often contain fluid inclusions entrapped during crystal  
157 growth (Böhlke & Irwin, 1992; Jamieson et al., 2016). Weber et al. (2016) characterized the  
158 fluid inclusions existing in barite which had earlier been used in the Ra uptake experiments of  
159 Curti et al. (2010), Klinkenberg et al. (2014) and Brandt et al. (2015). Nano-scale fluid  
160 inclusions filled with water and NaCl have been found to be arranged in layers by applying a  
161 complimentary approach of transmission electron microscopy (TEM) methods and atom  
162 probe tomography (APT).

163 Here, we present a detailed electron microscopy and focused ion beam study addressing the  
164 temporal evolution of Ra uptake by pre-existing barite with a focus on the internal  
165 microstructure and the distribution of Ra during the different uptake stages. By applying  
166 TEM techniques in 2D in combination with a focused ion beam and scanning electron  
167 microscopy (FIB-SEM) analysis in three spatial dimensions on samples taken at different  
168 times of the Ra uptake, we provide essentially a four-dimensional description of the uptake  
169 process.

170

## 171 **2. Materials and Methods**

### 172 **2.1 Barite samples from batch-type Ra uptake experiments**

173 A batch type experiment was carried out with the aim of preparing samples for a detailed  
174 microscopic study of the temporal evolution of the internal microstructure of barite during Ra  
175 uptake. The setup of the batch-type recrystallization experiment was identical to that  
176 described in Klinkenberg et al. (2014). During the experiment, a synthetic high-purity barite  
177 (XR-HR-10) from Sachtleben Chemie® GmbH (SL barite) was put into contact with a



178 Ra-containing solution. The initial experimental conditions were a solid to liquid ratio of  
179 0.5 g/L and a  $^{226}\text{Ra}$  concentration in solution of  $5 \cdot 10^{-6}$  mol/L. The concentration of  $^{226}\text{Ra}$  in  
180 solution was analyzed using Gamma-Spectroscopy after filtering using a 10,000 Da Advantec  
181 ultrafilter.

182 Parallel to the sampling of the aqueous solution, solid samples were taken from each stage  
183 of the experiment and prepared on a Si-wafer after washing with iso-propanol for electron  
184 microscopy according to the procedure described in Klinkenberg et al. (2014). For  
185 comparison, a barite sample taken after 602 days from the experiment presented as SL  
186 0.5 g/L in Brandt et al. (2015) was analyzed as well (Fig. 1). Reference experiments without  
187 Ra were carried out to separate the possible effects of recrystallization with and without Ra.

188

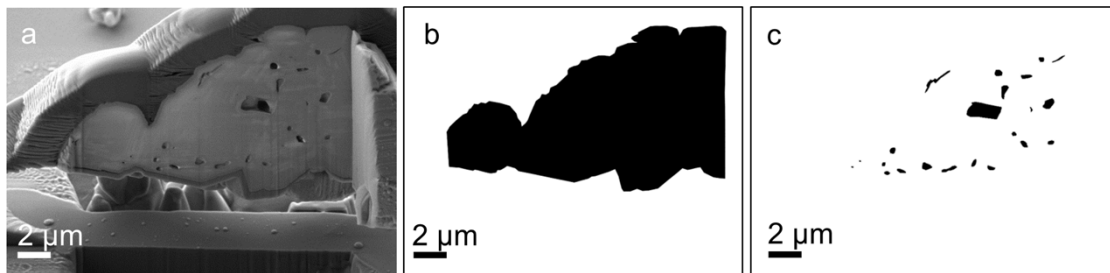
## 189 **2.2 Characterization of the solids**

### 190 **2.2.1 FIB cross-section preparation and image analysis**

191 Preparation procedures are described in detail in Weber et al. (2016) and in the references  
192 provided therein. Cross-sections along the longest particle axis were prepared by applying a  
193 variety of FIB instruments. Ra-containing samples were prepared in a Zeiss NVision40 cross  
194 beam workstation (Carl Zeiss AG, Germany) located in a controlled area, whereas Ra-free  
195 reference samples were prepared in two different but equivalent instruments, a FEI Helios  
196 NanoLab 460F1 (Kruth et al., 2016) or a FEI Helios Nanolab 400S (Meertens et al., 2016;  
197 FEI Company, The Netherlands).

198 The macropores within the barite samples were evaluated by the analysis of SEM images  
199 taken from FIB cross-sections. The areas comprising the complete particle and the areas  
200 corresponding to pores were separated and extracted by means of a contrast analysis (ImageJ)  
201 of the SEM images (Fig. 2). The area based macroporosity was calculated from the ratio of

202 the total particle and the macropore areas. A number of at least ten FIB cross-sections were  
203 prepared for this purpose and analyzed from each individual sample listed in Table 1.



204

205 Fig. 2. Image analysis for the determination of the area based macroporosity: (a) SEM image of a  
206 barite particle FIB section, (b) extracted area of the barite particle, (c) extracted area of macropores

207

### 208 2.2.2 FIB-SEM tomography

209 FIB-SEM tomography with the slice & view technique (Holzer et al., 2004) was performed  
210 using a FEI Helios NanoLab 460F1 FIB-SEM instrument (FEI Company, The Netherlands;  
211 Kruth et al., 2016) to obtain the 3D visualization of the macropore distribution within the  
212 initial SL barite prior the addition of Ra. Slices of several barite particles were cut parallel to  
213 the longest particle axis and studied by SEM using secondary electron (SE) images. A  
214 30 kV / 2.5 nA Ga ion beam was applied to cut two trenches on both sides of the particle and  
215 then a third trench from the front of the area of interest to expose the first segment of the  
216 slice-and-view section.

217 Tomographic data sets were acquired by sequential cutting of in total 734 slices of  
218 approximately 20 nm thickness with a 2.5nA ion beam and subsequent SEM. Each cross-  
219 section was imaged in mirror detection (MD) mode as well as by a through-the-lens back-  
220 scattered (TLD-BS) detector using a 2 kV/ 0.4 nA electron beam with a scan step size of  
221 7.68 nm. The recorded SEM images were combined as a stack in a single three-dimensional  
222 volume by the tools available in the AVIZO 9.0.0 software package (FEI Company, The

223 Netherlands). Subsequently, the segmentation of the pore space was performed with the same  
224 software package.

225

### 226 **2.2.3 TEM Sample preparation by focused ion beam (FIB)**

227 TEM lamellae with a thickness below 100 nm were cut from the barite particles using a  
228 focused  $^{69}\text{Ga}^+$  ion beam (FIB) instrument. The same variety of instruments as used for FIB  
229 cross-section preparation was used here. A detailed description of the barite sample  
230 preparation procedures applied in this study for particle cross-sections and cross-section TEM  
231 lamellae is given in Weber et al. (2016). A minimum of two TEM lamellae of each sampling  
232 date was prepared and thoroughly characterized.

233

### 234 **2.2.4 Transmission electron microscopy (TEM)**

235 A FEI Tecnai G<sup>2</sup> electron microscope (FEI Company, The Netherlands) (Luysberg et al.,  
236 2016) operated at 200 kV accelerating voltage was used to record selected area electron  
237 diffraction (SAED) patterns and scanning transmission electron microscopy (STEM) images  
238 using a high-angle annular dark-field (HAADF) detector.

239 Elemental maps were acquired by energy dispersive x-ray (EDX) mapping using a FEI  
240 Titan G<sup>2</sup> 80 – 200 electron microscope (Kovacs et al., 2016) equipped with an EDX system in  
241 the ChemiSTEM<sup>TM</sup> design (FEI Company, The Netherlands) operated at 80 kV accelerating  
242 voltage. The ChemiSTEM<sup>TM</sup> design consists of an annular orientation of four large-area,  
243 windowless SDD detectors in the Super-X<sup>TM</sup> geometry around the sample area, resulting in  
244 improved detection limits compared to the standard design.

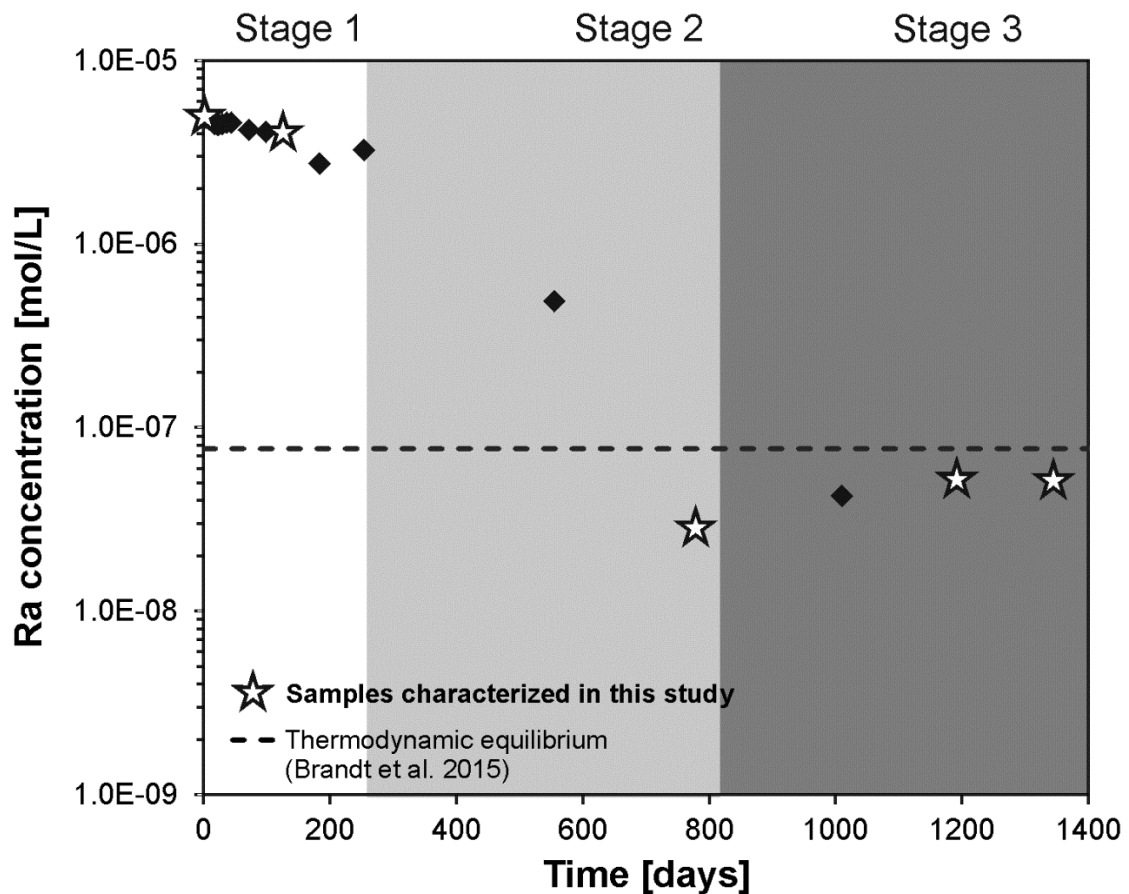
245

## 246 **3. Results and Discussion**

### 247 **3.1 Macroscopic results**

248 The macroscopic results of the Ra-uptake experiment conducted in this study are displayed  
249 in Fig. 3 and summarized in Table 1. The macroscopic results obtained in this study are in  
250 good agreement with a large number of experiments discussed in detail in Brandt et al.  
251 (2015). In particular, these data sets indicate a Ra uptake of more than 99 % into the solid  
252 after stage 2, and the Ra concentration reaches a plateau in stage 3 (broken line in Fig. 3;  
253 Brandt et al., 2015), which was earlier discussed as approach to equilibrium between solid  
254 and solution. The Ra/Ba ratio after reaching equilibrium state is about  $2 \cdot 10^{-3}$  and therefore,  
255 the molar volume change and the change in solubility associated with the replacement  
256 process can be considered negligible. As a conclusion, no internal microstructural changes  
257 would be expected based on the molar volume change or the difference of solubility between  
258 parent and resulting phase.

259 Several representative solid samples for further analyses were taken in order to follow the  
260 possible internal changes related to the stages of Ra-uptake: two samples in stage 1, one  
261 sample at the minimum Ra-concentration at stage 2 and two samples within stage 3. For  
262 comparison, a sample from the study of Brandt et al. (2015) taken at stage 3 was included in  
263 the analyses to make a direct link to this study and to the earlier study of Klinkenberg et al.  
264 (2014).



265

266 Fig. 3. Temporal evolution of the aqueous Ra concentration in the Ra-uptake experiment providing  
 267 the samples for the microscopic study. Sampling of solid samples is marked with a ★. The  
 268 thermodynamic equilibrium concentration was calculated using an interaction parameter of  $a_0 = 1$   
 269 (Vinograd et al., 2013).

270

271 Table 1

272 Overview of solid samples from Ra uptake experiments and the Ra-free reference experiment.

273 Experiment 2 was discussed in detail in Brandt et al. (2015) and Klinkenberg et al. (2014).

Sample	Experiment	Time [days]	Ra concentration in solution [mol/L]	Stage
Initial barite		0	0	0
Exp1_1a	Experiment 1	1	$4.90 \cdot 10^{-6}$	1
Exp1_1b	Experiment 1	126	$4.03 \cdot 10^{-6}$	1
Exp1_2	Experiment 1	779	$2.82 \cdot 10^{-8}$	2

Exp1_3a	Experiment 1	1192	$5.20 \cdot 10^{-8}$	3
Exp1_3b	Experiment 1	1345	$5.20 \cdot 10^{-8}$	3
Exp2_3	Experiment 2	602	$5.03 \cdot 10^{-8}$	3
Ref1	Reference 1	1	0	
Ref2	Reference 1	127	0	
Ref3	Reference 1	505	0	
Ref4	Reference 1	898	0	

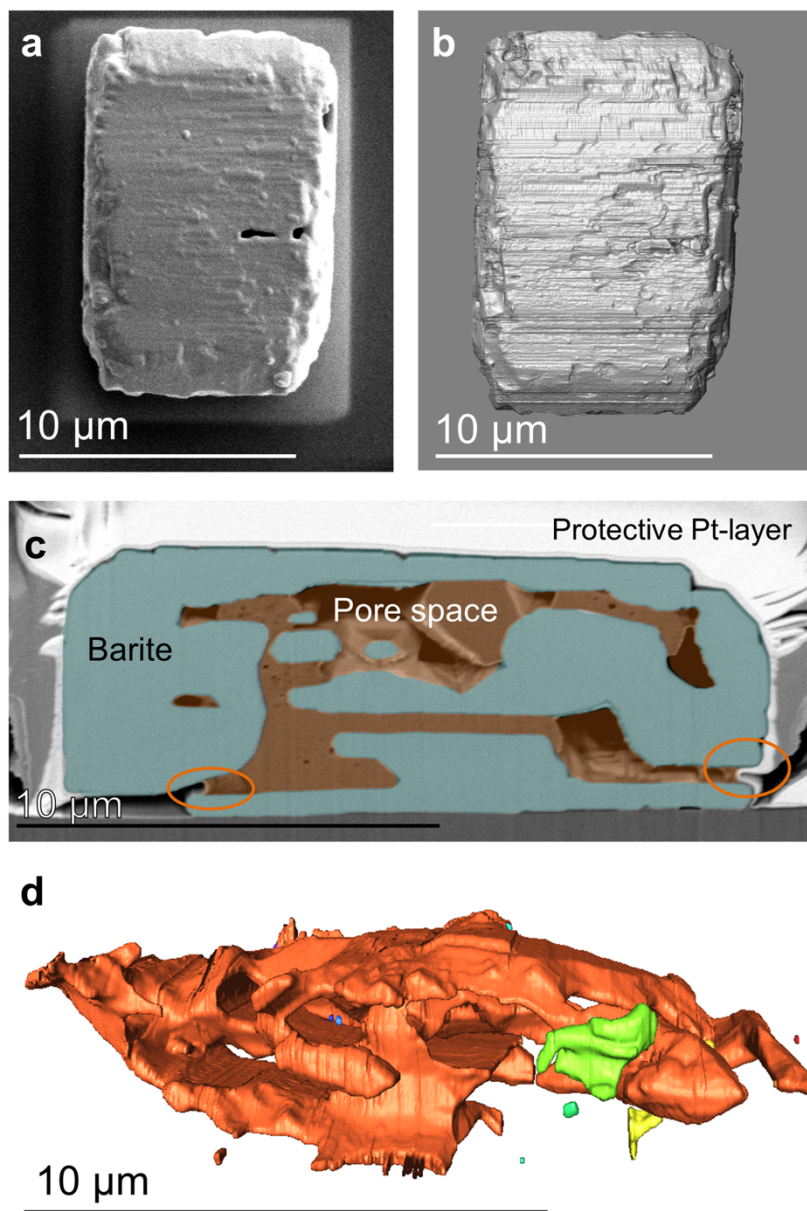
274

275

### 276 **3.2 Macro porosity and connectivity of pores and their temporal evolution of Ra-free** 277 **reference samples**

278 Numerous cross-sections of the initial barite were already prepared and discussed in Weber  
279 et al. (2016). The typical microstructure of this barite comprises macropores and nanometer  
280 scaled pores. Fast pathways for the uptake of Ra via pores would require a connection of  
281 pores and openings in the particle surface. However, so far the existence of an open pore  
282 network could not be shown based on single cross-sectional views. Therefore, FIB-SEM  
283 tomography was carried out here on an initial barite and on a grain of a reference experiment  
284 without radium after 127 days in solution. In contrast to individual FIB cross sections, the  
285 tomography technique provides a three-dimensional (3D) reconstruction of the macropore  
286 network as shown in Fig. 4. For example, Fig. 4a shows the SEM image of the initial SL  
287 barite particle and Fig. 4b the reconstructed particle based on the segmentation. Three pores  
288 in the barite surface are visible which indicate the presence of internal porosity with a  
289 connection to the outside. Typical for all initial barite samples analyzed by FIB cross-sections  
290 and tomography is a connected network of macropores (Fig. 4d) which is at least partially  
291 connected to the particle surfaces (Fig. Fig. 4c, orange circles). Compared to the particle  
292 volume, some of these pores provide a large entrance for Ra to enter from the aqueous phase  
293 by fluid diffusion and reach far into the inside of the particle. In some particles connected  
294 macropores were observed, opening up a significant reactive surface area in addition to the

295 outer particle surface. In addition to the figures presented here, a video of the 3D  
296 reconstruction is available in the supplemental information showing the three-dimensional  
297 distribution of the macroporosity.



298

299 Fig. 4. FIB tomography of an initial SL barite particle: a) Top view SEM image of the SL barite  
300 particle. b) Top view of the reconstructed particle based on the segmentation of the outer material. c)  
301 Cross-section of the reconstructed volume showing the barite particle material selected for  
302 segmentation in blue and the selected pore space in orange. The orange circles highlight the open

303 macropores and the connection of the internal pores to the bulk fluid. d) Side view of the segmented  
304 pore volume. Connected macropores are highlighted in the same color.

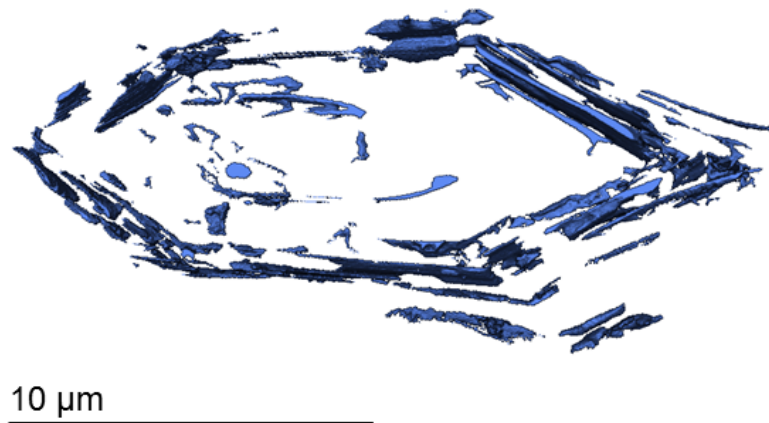
305

306 Under the hypothesis that macropores are a possible pathway of Ra into barite via diffusion  
307 within the pore solution, an inhomogeneous uptake of Ra into barite would be expected  
308 owing to our observation that not all macropores are connected. Accordingly, the uptake may  
309 vary from particle to particle. Furthermore, it should be considered that one third of the 2D  
310 barite cross-sections did not show any porosity. In comparison to the initial sample, similar  
311 observations were made for the reference sample after 127 days. Connected macropores were  
312 observed in the FIB-SEM tomography of this sample as well, which were oriented mostly  
313 parallel to the outer surfaces of the particle (Fig. 5).

314 The evolution of the macroporosity was analyzed in detail by image analysis of FIB cross-  
315 sections from day 1, 127, 505 and 898 in order to identify whether the macroporosity inside  
316 the barite changes during recrystallization. The resulting area-based porosity is given in Table  
317 2. No error is specified here as the determination is only semi-quantitative due to the  
318 limitations imposed by 2D cutting effects. Despite of these limitations, it should be still  
319 possible to observe a relative trend in the area-based porosity. However, the present data does  
320 not show a clear evolutionary trend of the porosity.

321





322

323 Fig. 5. FIB tomography reconstruction of a particle after equilibration in 0.1 mol/L NaCl for 127 days.

324

325 Table 2 Evolution of macroporosity inside Ra-free reference barite particles based on image analysis.

Sample	Time [days]	Number of analyzed cross-sections	Area-based porosity [%]
Ref1	1	11	1.5
Ref2	127	11	1.7
Ref3	505	5	2.3
Ref4	898	11	2.0

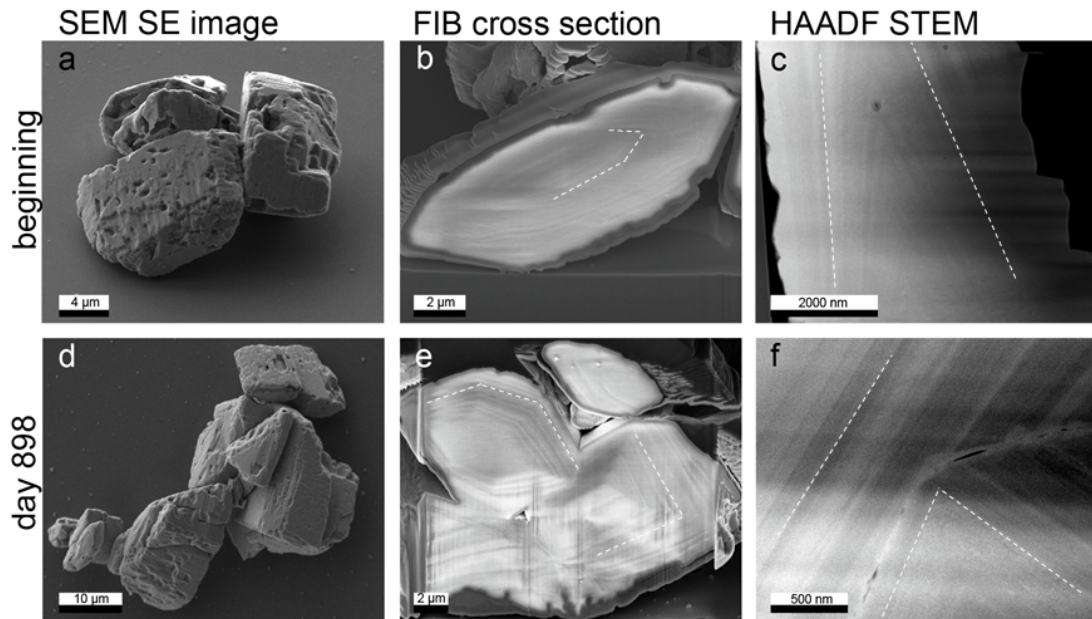
326

### 327 3.3 Temporal evolution of the nano-scaled pores in the Ra-free reference samples

328 In addition to the evolution of the macropores, nanometer scale pores were identified  
 329 within barite samples taken at defined times during long-term experiments of up to 898 days  
 330 (Fig. 6). Similar as described in Weber et al. (2016), SEM observations of the outside of all  
 331 Ra-free reference samples (Fig. 6a,d) as well as the detailed observations in FIB cross-  
 332 sections (Fig. 6b,e) and HAADF STEM images (Fig. 6c,f) indicate the presence of a layered  
 333 structures formed by nano-scale pores. Dark HAADF STEM contrast indicate a high content  
 334 of nano-scale porosity whereas bright areas indicate absence of nano-scale porosity. Within

335 898 days, the main change that was observed on the outside of the particles is a smoothening  
336 of the particle surfaces and a tendency of particles to merge. However, very little or no  
337 change of the internal microstructure was observed. Even after 898 days the layered internal  
338 structures are clearly visible (Fig. 6e, f). The width of the layered structures, their orientation  
339 and other characteristic features are very well comparable at all stages of the reference  
340 experiments. This can be taken as an indication of a very stable internal microstructure of  
341 barite. The high stability of fluid inclusions in barite was also recently reported by Jamieson  
342 et al. (2016) where they were proposed to preserve the conditions of physical and chemical  
343 processes at the seafloor. However, the same barite powders as used in the presented  
344 experiments appear to undergo significant recrystallization on the time scale of the  
345 experiment according to  $^{133}\text{Ba}$  tracer experiments (Bosbach et al., 2010; Curti et al., 2010).  
346 Therefore, either the recrystallization in Bosbach et al. (2010) and Curti et al. (2010) may  
347 have been triggered by the presence of  $^{133}\text{Ba}$ , or the fluid inclusions are stable against the  
348 recrystallization of barite itself.

349



350

351 Fig. 6. Temporal evolution of the internal microstructure of SL barite from the Ra-free reference  
 352 experiment at the beginning (a – c) and after 898 days (d – f). SEM images of the barite particles are  
 353 given in (a) and (d), while (b) and (e) show SEM images of FIB cross-sections. The nano-scale  
 354 porosity is visible as a layered structure in HAADF STEM images (c) and (f), where dashed lines  
 355 trace back the layered structure.

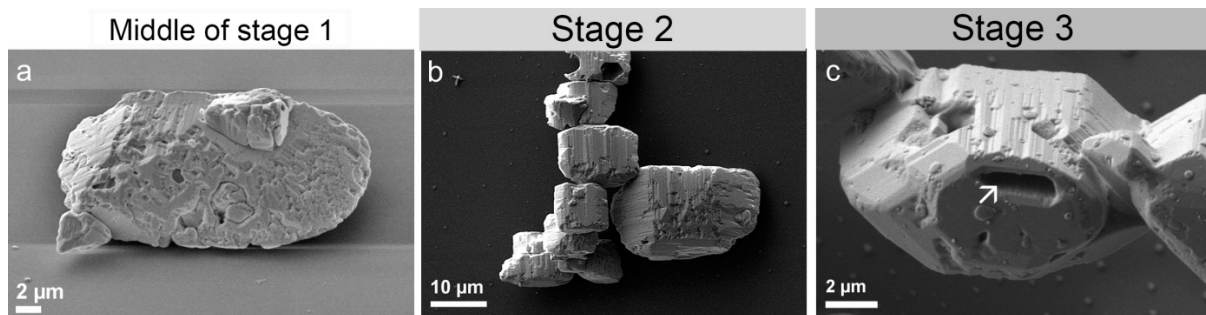
356

### 357 3.4 Temporal evolution of barite samples from $^{226}\text{Ra}$ uptake experiments

358 During stage 1 no significant changes of the external microstructure could be detected by  
 359 SEM imaging. At the middle of stage 1 (day 126), the surface of the barite particle in Fig. 7a  
 360 shows many pores and a very irregular rough surface. The particles remained well separated.

361 At stage 2, the particles started growing together, forming chains (Fig. 7b). In most of the  
 362 cases they were attached to each other either at the  $\{210\}$  surfaces or at the  $\{100\}$  surfaces. In  
 363 a recently published study of Zhang et al. (2017), Van-der-Waals forces are considered as  
 364 reason for crystallographic oriented attachment of particles. During the Ra uptake and barite  
 365 recrystallization until stage 3, the barite surface is smoothed (Fig. 7c), and fewer pores than  
 366 in the previous stages were observed. Later in stage 3, when approaching equilibrium, long

367 chains of particles have formed building a complex three-dimensional structure. In addition,  
368 the particles exhibit a further developed euhedral shape compared to the beginning of  
369 equilibration. Still large pores are visible in the barite particle surface as indicated in Fig. 7c.  
370



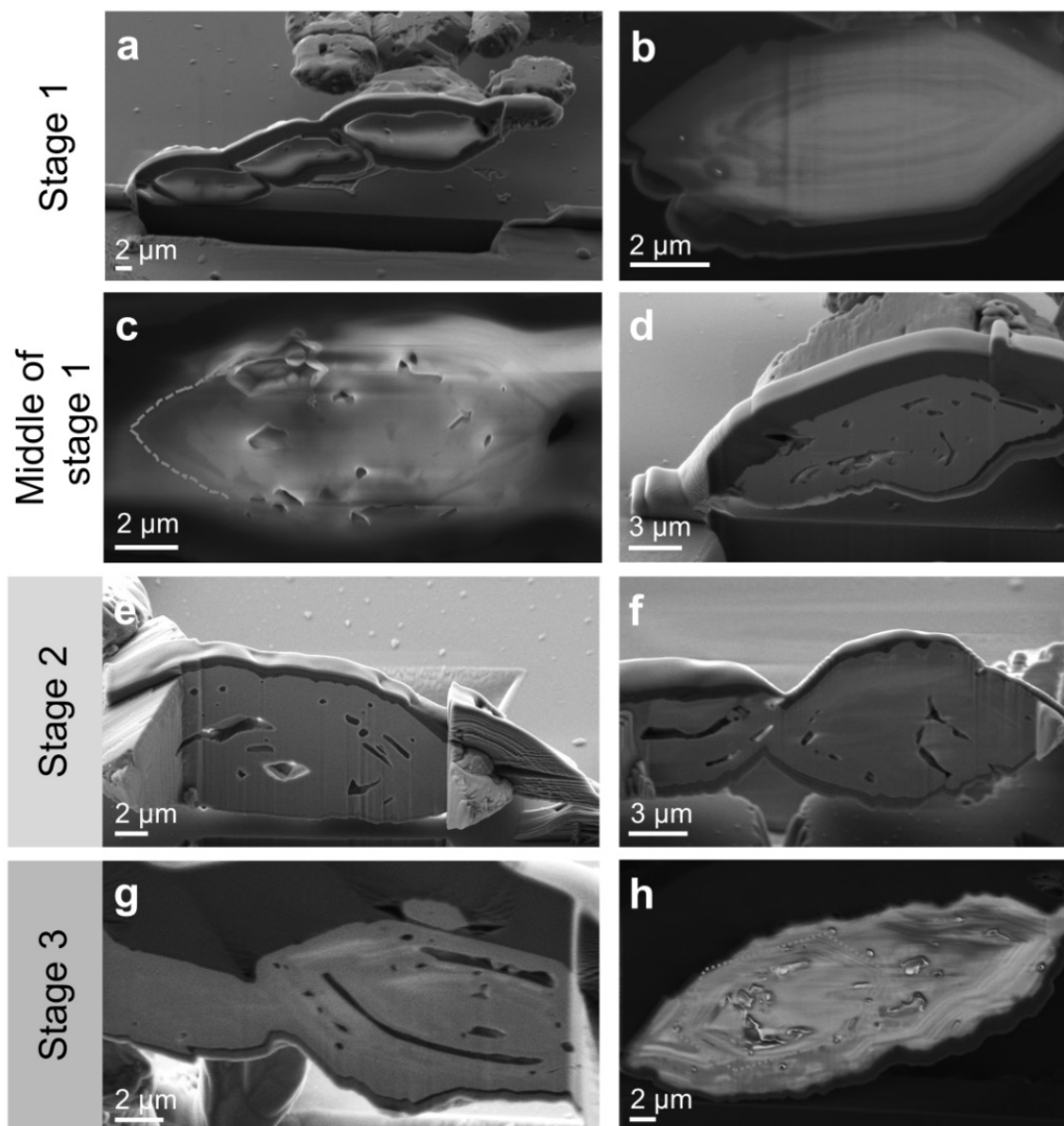
371  
372  
373 Fig. 7. SEM images showing the effects of recrystallization of barite in the presence of Ra. At the end  
374 of stage 1 (a), the crystal surfaces are very rough and many pores are visible. The Ra-barites start  
375 growing together and show a smoothing of the crystal surfaces at stage 2 (b). The particle shape  
376 evolves more towards euhedral barite shape. At the stage 3 (c), the Ra-barite particles are grown  
377 together. Crystal surfaces are smoother with new precipitates on them; the arrow indicates a pore.

378  
379 Fig. 8 shows FIB cross-sections of radiobarites at different stages of the Ra-uptake. In the  
380 presence of Ra, the internal microstructure of the barite grains becomes unstable and changes  
381 significantly already during stage 1 of the Ra uptake, while their external structure remains  
382 essentially unchanged. The internal microstructure now contains larger pores while the  
383 layered nano-scale pore structures are partially or even completely eliminated (Fig. 8c). In  
384 contrast to the Ra-free reference, the area-based macroporosity reaches a clear maximum in  
385 the middle of stage 1 (Table 3). This can be taken as an indication that the nanometer-scale  
386 pores coalesce to macropores during the Ra uptake, minimizing the surface free energy. The  
387 HAADF STEM images displayed in Fig. 9a-c shows the remaining layered structure  
388 consisting of nano-scale pores as well as of macropores in direct vicinity.

389 At stage 2, when the minimum Ra concentration in solution is reached, further coalescing  
390 of the nano-scaled pores has led to the formation of additional macropores and no layered  
391 structure could be observed in HAADF STEM and SEM images of FIB cross sections  
392 anymore (Fig. 8e,f; Fig. 9d-f). In comparison, even later in the reference experiment, layered  
393 structures are still clearly visible (Fig. 6e,f). The FIB section at this stage of the Ra uptake  
394 indicates that some of the pores are oriented in the same direction as the former layered  
395 structures whereas some are also irregularly distributed within the barite particles (Fig. 8e,f).  
396 The area-based macroporosity at this stage has decreased from ca. 6.6 % back to 3.7 %  
397 (Table 3). Additionally, as discussed in the later part of this study, the uptake of Ra and its  
398 heterogeneous distribution could be indicated by brighter contrasts in HAADF STEM images  
399 (Fig. 9d-f, Fig. 10).

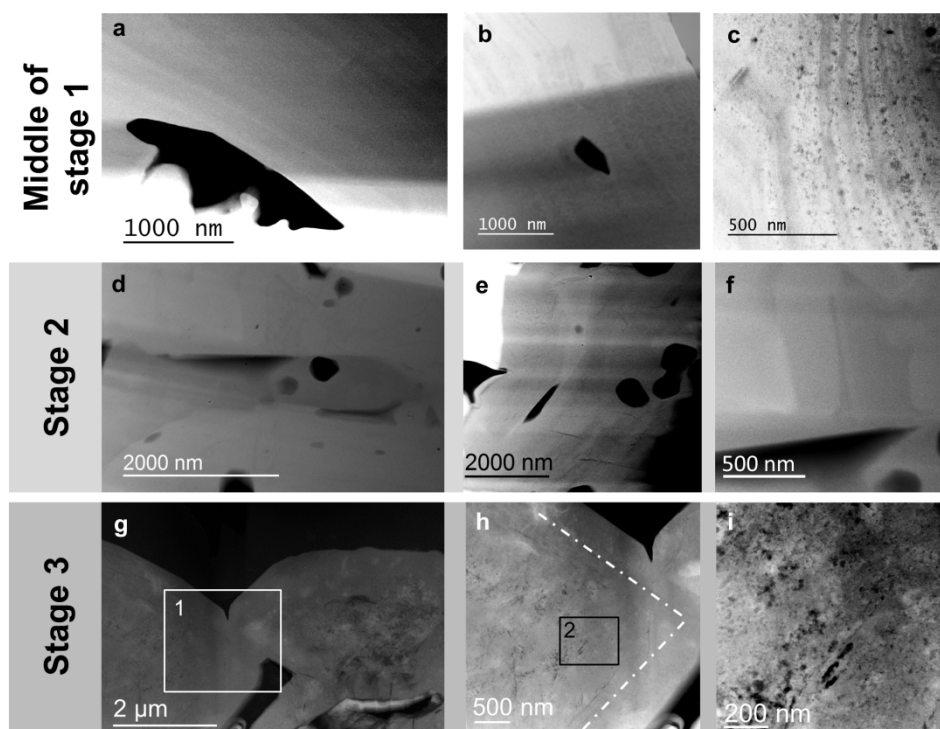
400 During the final stage 3 of the Ra uptake experiments, macropores of several micrometers  
401 in length which are typically oriented parallel to the outer crystal surfaces occur in some of  
402 the FIB cross-sections (Fig. 8 g). In the HAADF STEM images an outer rim of higher density  
403 becomes visible, most likely indicating the formation of coherent newly formed (Ba,Ra)SO<sub>4</sub>  
404 (Fig. 9 h). Inside this rim, areas of increased nano-scale porosity are observed (Fig. 9 i).  
405 Additional HAADF STEM and TEM images showing this dense rim and the newly formed  
406 inner nano-scale porosity are given in the Fig. S1 and S2 of the supplemental information.

407



408

409 Fig. 8. FIB-cross sections of Ra-barites from different stages. In stage 1, particles with macropores (a)  
 410 are present as well as particles with a layered structure (b). This layered structure starts to disappear in  
 411 the middle of stage 1 (c) and more elongated pores can be observed (d). At stage 2, hollow barite  
 412 cores are observed (e) as well as particles growing together (f). At stage 3, the macropores grow  
 413 together (g) and particles are completely grown together to new particles (h).



414

415

416 Fig. 9. HAADF STEM images of the Ra-barite sampled at different stages of recrystallization. The  
 417 Ra-barites from the middle of the stage 1 clearly display a layered structure (a) and (b). At higher  
 418 magnification (c), it is visible that the layers consist of larger nano-scale pores similar as observed in  
 419 the beginning of stage 1. At stage 2, no layered structure can be observed anymore (d) – (f). Visible  
 420 contrast variations could not be attributed to nano-scale porosity but could indicate an enrichment of  
 421 Ra. At the stage 3 (g), a massive outer rim is visible. The area (1) is magnified in (h) showing this  
 422 massive rim. The particles contain newly formed nano-scale porosity in the area (2) which is  
 423 magnified in (i).

424

425 Table 3 Evolution of area-based macroporosity during Ra uptake based on semi-quantitative image  
426 analysis.

Sample	Stage	Number of analyzed cross sections	Area-based porosity [%]
Exp1_1a	1 beginning	9	3.5
Exp1_1b	1 middle	12	6.6
Exp1_2	2	4	3.7
Exp1_3	3	25	2.3

427

428

### 429 **3.5 Temporal evolution of the spatial distribution of Ra**

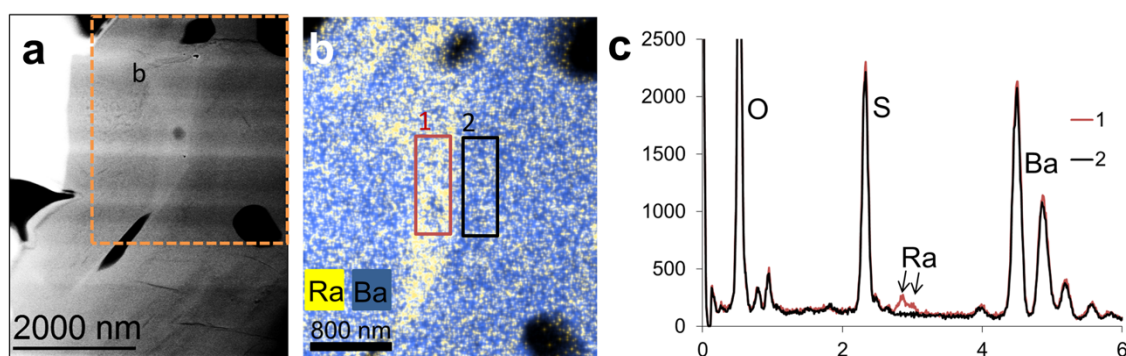
430 High resolution STEM-EDX measurements and mappings were performed to track the Ra  
431 uptake and (Ba,Ra)SO<sub>4</sub> solid-solution formation. No Ra was detected within FIB-lamellae of  
432 barite particles of sample Exp1\_1b taken within the first half of stage 1 with STEM-EDX.  
433 Based on the Ra-concentration of the corresponding aqueous solution sample, only a very  
434 small amount of Ra should be present inside the barite sample at this stage. Since no Ra was  
435 detected by EDX spectroscopy, the Ra-concentration inside the barite solid is probably below  
436 the detection limit at the first half of stage 1. In contrast, Ra was clearly identified with the  
437 same technique in sample Exp1\_2 taken at the time corresponding to the minimum Ra  
438 concentration in solution of stage 2 (Fig. 10). STEM-EDX mappings taken from the same  
439 sample indicate an inhomogeneous Ra and Ba distribution at this stage of the Ra uptake  
440 experiment (Fig. 10 b). The sample presented in Fig. 10a shows differences in the contrast  
441 indicating the presence of inhomogeneity. In this sample, the bright area is located between  
442 two pores. The EDX mapping shows a Ra distribution which qualitatively matches the  
443 HAADF contrast variations (Fig. 10b and c). A significant amount of Ra in the range of more  
444 than 1 at% is present in the yellow area of Fig. 11b. Higher Ra concentrations typically were  
445 observed near pores in the EDX mappings indicating that Ra appears to replace Ba (Fig. 11a).



446 Additional STEM-EDX mapping of samples from stage 2 demonstrating the inhomogeneous  
447 Ra distribution within the barite can be found in Fig. S3 - S5 of the supplemental information.

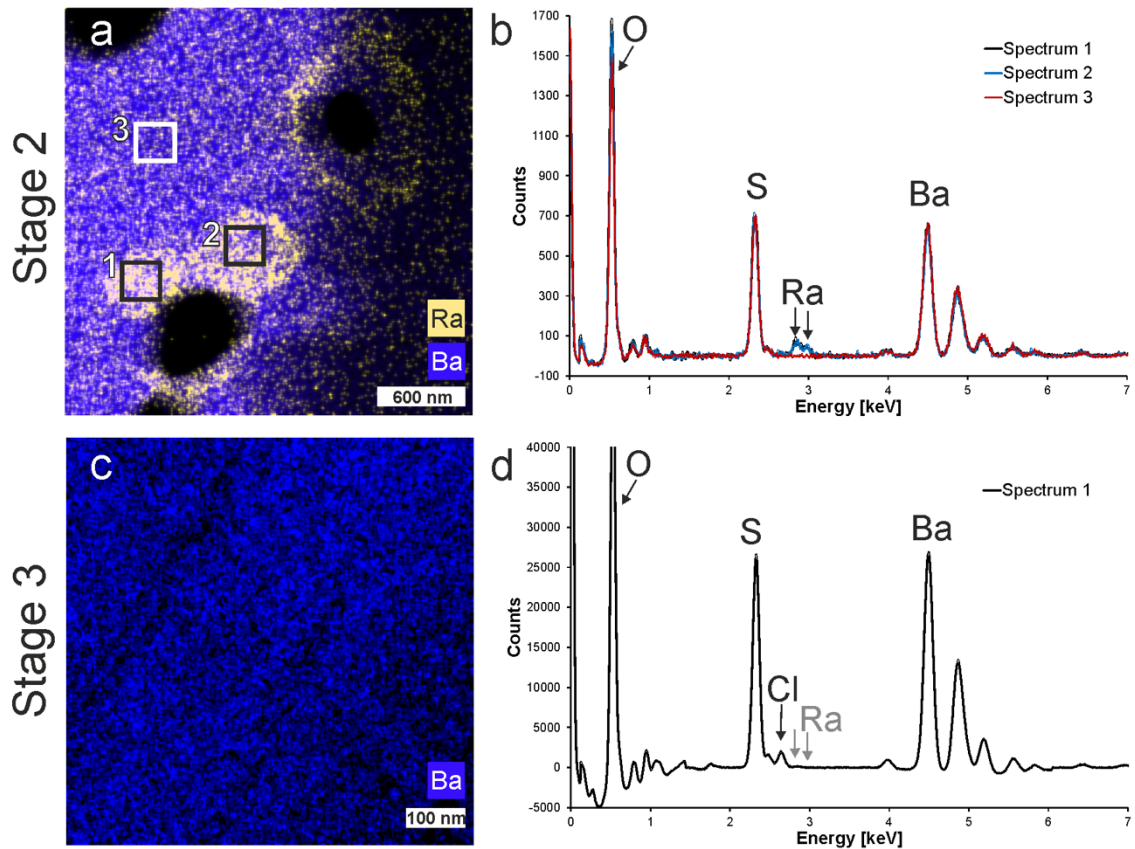
448 Fig. 11c shows the STEM-EDX mapping of the Ra containing sample at stage 3,  
449 corresponding to the approach of equilibrium between aqueous solution and solid. Based on  
450 mass balance between solid and solution and assuming a homogeneous distribution of Ra in  
451 the solid, the calculated Ra concentration of the barite particles was 60 ppm. Unfortunately,  
452 this is well below the detection limit of the applied EDX spectroscopy system. In the case of  
453 a homogeneous Ra distribution, consequently no Ra peak would be expected. The EDX  
454 spectrum corresponding to c confirms this expectation (Fig. 11d). Furthermore, the Ra-  
455 concentration in solution remained stable near the calculated equilibrium concentration  
456 during stage 3. Therefore, we deduce indirectly that Ra was distributed homogeneously in  
457 stage 3, i.e. a complete (Ra,Ba)SO<sub>4</sub> solid has formed, which is in equilibrium with the  
458 aqueous solution. Additional STEM-EDX measurements are given in Fig. S6 and S7 of the  
459 supplemental information.

460



461  
462 Fig. 10. Ra distribution inside the barite at stage 2. (a) HAADF-STEM image of sample Exp1\_2 taken  
463 at stage 2, (b) corresponding STEM-EDX mapping of the area indicated in (a) by broken lines, (c)  
464 EDX-STEM spectra taken from the areas (1) and (2) in (b). The spectrum of area 1 shows clear signal  
465 of Ra, whereas no Ra signal is visible in spectrum 2.

466



467

468 Fig. 11. Temporal evolution of the radium distribution from stage 2 to stage 3. (a) STEM-EDX  
 469 mapping of Ra (yellow) and Ba (blue) at stage 2 (sample Exp1\_2). The black areas are the  
 470 macropores. (b) EDX spectra of the labeled areas 1, 2, and 3 (c) STEM-EDX mapping of barium at  
 471 stage 3 (sample Exp2\_3) (d) corresponding EDX spectrum of the whole area, no Ra signal detected.  
 472 The expected positions of the Ra-L peaks in the spectrum are marked by gray arrows.

473

474

#### 475 4. Summary and conclusion

476 New insights into the mechanism of the Ra uptake into barite were obtained by comparing  
 477 barite and Ra-barite samples applying a state-of-the-art high resolution microscopic  
 478 approach. Characteristic for the initial barite sample was a connected macroporosity offering  
 479 a fast pathway for Ra into the particle volume via fluid diffusion. The evolution of the

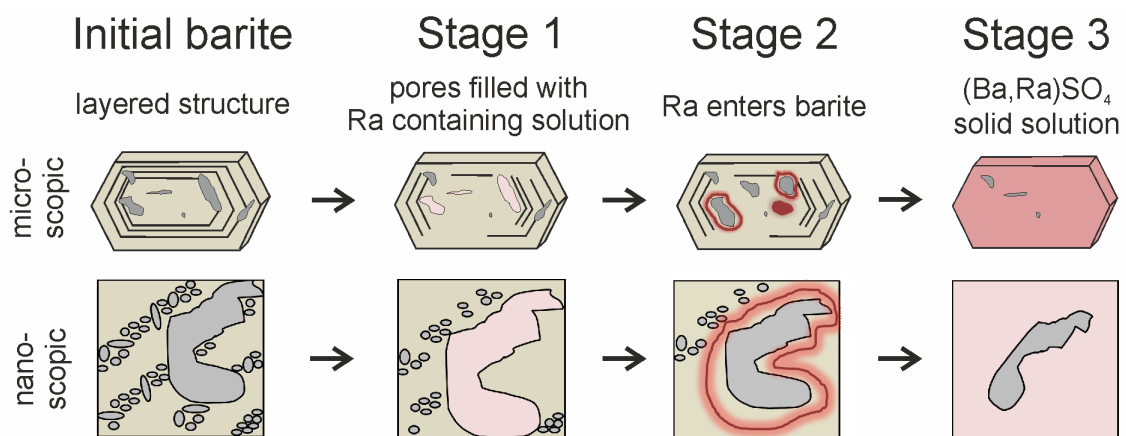
480 microstructure and the Ra distribution within barite was characterized at different stages of  
481 the Ra-uptake in order to understand the uptake mechanism.

482 In the presence of Ra, the surfaces of the barite samples became smoother with time,  
483 similar to the samples of the Ra-free recrystallization experiments. For the latter samples,  
484 also no significant changes were observed for the internal microstructure, even after  
485 recrystallization times of up to 898 days. In contrast to that, the overall porosity of the barite  
486 which was recrystallized in the presence of Ra changed in several steps: At the beginning, the  
487 nano-scale fluid inclusions disappeared, probably due to coalescing to new macropores,  
488 which could be favorable in the context of surface energy minimization. Later, the Ra-barite  
489 particles contained a dense rim structure with no porosity and an inner core of nano-scale  
490 porosity. In addition, the amount of macroporosity increased temporarily at stages 1 and 2,  
491 and was finally reduced again to a similar level as observed in the initial and reference  
492 samples. Energy minimization can be considered as a reason for reduction of macroporosity  
493 after the minimum observed in the radium concentration in solution. In addition, some  
494 available studies suggest that the reactivity of nanopores differs greatly from that of other  
495 pores (Stack, 2014, Stack, 2015). Therefore, the presence of nano-scaled fluid inclusions in  
496 the starting material could provide additional energy triggering the exchange process.

497 During stage 1, no Ra was detected in the solid by EDX spectroscopy. Ra may have  
498 migrated within the aqueous phase into the barite samples and may be still contained within  
499 the macropores. During stage 2, Ra was distributed inhomogeneously within the barite  
500 crystals. It was found to be concentrated in rims around some macropores. During stage 3, the  
501 Ra concentration was below the detection limit of EDX spectroscopy. A homogeneous Ra  
502 distribution in the particles and a stable aqueous Ra concentration support the conclusion that  
503 a thermodynamic equilibrium was reached at stage 3.

504 In summary, the mechanism of Ra uptake into barite appears to be a combination of Ra  
 505 diffusion through macropores into the crystal volume and a dissolution-precipitation from  
 506 the inside to the outside of the particles leading to a homogenous Ra distribution (Fig. 12). At  
 507 the scale of the experiments, residual porous structures on the inside of the particles remain,  
 508 although the solution composition approaches the predicted equilibrium of this solid-solution  
 509 aqueous solution system.

510



511

512 Fig. 12. Schematic summary of the process of Ra uptake into barite. Evolution of the micro/nano  
 513 structure in the presence of Ra.

514

515 Our results indicate that barite can be destabilized and significantly reconstructed internally  
 516 in the presence of a Ra-containing aqueous solution even though it appears to be quite stable  
 517 and close-to-equilibrium from the outside. The reactivity of the barite powders containing  
 518 fluid inclusions as investigated here could be utilized to directly remediate Ra from aqueous  
 519 solution into a thermodynamically stable form or to stabilize (Ba,Ra)SO<sub>4</sub> precipitated via co-  
 520 precipitation. The results also indicate that it is possible to take up more Ra into barite than  
 521 thermodynamically stable, leading to inhomogeneities of the Ra concentration within barite  
 522 particles. During the course of further equilibration, it can be expected that such (Ba,Ra)SO<sub>4</sub>  
 523 solid solutions which may be formed via co-precipitation in contact with a Ra-free solution

524 will release the surplus of Ra over a long time until equilibrium is reached. In this case, the  
525 addition of barite would keep the Ra in solution stable at a very low level.

526 Finally, regarding the implementation of the (Ba,Ra)SO<sub>4</sub> solid solution into safety  
527 assessments for deep geological disposal of spent nuclear fuel, the details of the Ra uptake in  
528 barite need to be understood. From the presented results, the attribution of the final steady  
529 state of the Ra concentration in solution to a homogeneous solid allows to take credit from  
530 this system.

531

532

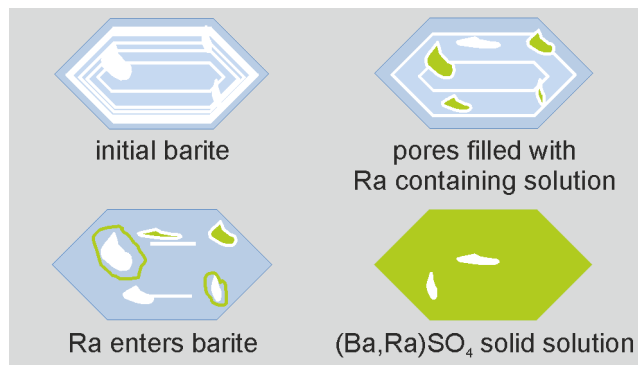
### 533 **Acknowledgements**

534 Prof. J. Mayer is acknowledged for his scientific input and discussion of TEM results. We  
535 are grateful to D. Meertens and A. Savenko for their support with the FIB preparation. Dr.  
536 Roland Schierholz is acknowledged for access to the analysis computer for the 3D  
537 tomography. The Swedish Nuclear Fuel and Waste Management Agency (Svensk  
538 Kärnbränslehantering Aktiebolag) is acknowledged for partially financing of this study. J.  
539 Barthel and M. Kruth acknowledge funding within the core facilities initiative of the German  
540 Research Foundation (DFG) under the grant number MA 1280/40-1. We are grateful to Dr.  
541 G. Deissmann for the fruitful discussions.

542

543

544 **Graphical abstract**



545

546

547 **Highlights:**

548 (maximum 125 characters, including spaces, per bullet point)

- 549
- Completely different evolution of the microstructure in Ra uptake and Ra-free
- 550 recrystallization experiments observed
- 551
- Complete re-equilibration from a temporary, inhomogeneous Ra distribution to a
- 552 homogeneous (Ba,Ra)SO<sub>4</sub> solid solution
- 553
- Uptake of Ra into barite by a special case of dissolution-reprecipitation process
- 554 proceeding from the inside of the particle to the outside in addition to the uptake from
- 555 the outside

556

557 **AUTHOR INFORMATION**

558 **Corresponding Author**

559 \* New affiliation: Oak Ridge National Laboratory, Phone: 865-576-7184, E-Mail:

560 weberj@ornl.gov

561

562 **References**

563 Al Attar, L., Safia, B., Abdul Ghani, B., Chemical composition of scales generated from oil  
564 industry and correlation to radionuclide contents and gamma-ray measurements of  
565  $^{210}\text{Pb}$ . *Environ. Pollut.* **2016**, 210, 246–252. DOI: [10.1016/j.envpol.2015.12.007](https://doi.org/10.1016/j.envpol.2015.12.007)

566 Atree-Williams, A., Pring, A., Ngothai, Y., Brugger, J., Textural and com-positional  
567 complexities resulting from coupled dissolution–reprecipitation reactions in  
568 geomaterials: *Earth-Science Reviews*, **2015**, 150, 628-651. DOI:  
569 [10.1016/j.earscirev.2015.08.013](https://doi.org/10.1016/j.earscirev.2015.08.013)

570 Attallah, M. F., Hamed, M. M., El Afifi, E. M., Aly, H. F., Removal of  $^{226}\text{Ra}$  and  $^{228}\text{Ra}$  from  
571 TENORM sludge waste using surfactants solutions. *J. Environ. Radioact.* **2015**, 139,  
572 78–84. DOI: [10.1016/j.jenvrad.2014.09.009](https://doi.org/10.1016/j.jenvrad.2014.09.009)

573 Böhlke, J. K., Irwin, J. J., Brine history indicated by argon, krypton, chlorine, bromine, and  
574 iodine analyses of fluid inclusions from the Mississippi Valley type lead-fluorite-barite  
575 deposits at Hansonburg, New Mexico. *Earth Planet. Sci. Lett.* **1992**, 110, 51–66. DOI:  
576 [10.1016/0012-821X\(92\)90038-W](https://doi.org/10.1016/0012-821X(92)90038-W)

577 Bosbach, D., Boettle, M., Metz, V. SKB Technical Report. 2010, TR-10-43.

578 Blount, C.W. Barite solubilities and thermodynamic quantities up to 300 °C and 1400 bars.  
579 *Amer. Mineral.*, **1977**, 62, 9-10.

580 Brandt, F., Curti, E., Klinkenberg, M., Rozov, K., Bosbach, D., Replacement of barite by a  
581 (Ba,Ra)SO<sub>4</sub> solid solution at close-to-equilibrium conditions: A combined experimental  
582 and theoretical study. *Geochim. Cosmochim. Acta* **2015**, 155, 1–15. DOI:  
583 [10.1016/j.gca.2015.01.016](https://doi.org/10.1016/j.gca.2015.01.016)

584 Bruno, J., Bosbach, D., Kulik, D., Navrotsky, A., *Chemical thermodynamics of solid*  
585 *solutions of interest in nuclear waste management: a state-of-the-art report*; Mompean,

586 F. J.; Illemassene, M.; Perrone, J., Eds.; OECD Nuclear Agency (NEA): Paris, France,  
587 2007; Vol. 10.

588 Chalupnik, S., Wysocka, M. Radium removal from mine waters in underground treatment  
589 installations. *J. Environ. Radioact.* **2008**, *99*, 1548–1552. DOI:  
590 [10.1016/j.jenvrad.2007.12.024](https://doi.org/10.1016/j.jenvrad.2007.12.024)

591 Curti, E., Fujiwara, K., Iijima, K., Tits, J., Cuesta, C., Kitamura, A., Glaus, M., Müller, W.  
592 Radium uptake during barite recrystallization at 23±2 °C as a function of solution  
593 composition: An experimental <sup>133</sup>Ba and <sup>226</sup>Ra tracer study. *Geochim. Cosmochim. Acta*  
594 **2010**, *74*, 3553–3570. DOI: [10.1016/j.gca.2010.03.018](https://doi.org/10.1016/j.gca.2010.03.018)

595 Gorski, C.A., Fantle, M.S., Stable Mineral Recrystallization in Low Temperature Aqueous  
596 Systems: A Critical Review. *Geochim. Cosmochim. Acta* **2016**, *198*, 439-465. DOI:  
597 [10.1016/j.gca.2016.11.013](https://doi.org/10.1016/j.gca.2016.11.013)

598 Grandia, F., Merino, J., Bruno, J. *Assessment of the radium-barium co-precipitation and its*  
599 *potential influence on the solubility of Ra in the near-field*, SKB Technical Report TR-  
600 08-07, SKB: Stockholm, Sweden, 2008.

601 Hanor, J.S. Barite-celestine geochemistry and environments of formation. *Review in*  
602 *Mineralogy and Geochemistry*, **2000**, *40.1*, 193-275. DOI: 10.2138/rmg.2000.40.4

603 Heberling, F., Paulig, L., Nie, Z., Schild, D., Finck, N. Morphology Controls on Calcite  
604 Recrystallization. *Environ. Sci. Technol.* **2016**, *50*, 11735–11741. DOI:  
605 10.1021/acs.est.6b04011

606 Hellmann, R., Cotte, S., Cadel, E., Malladi, S., Karlsson, L.S., Lozano-Perez, S., Cabié, M.,  
607 Seyeux, A., Nanometre-scale evidence for interfacial dissolution–reprecipitation  
608 control of silicate glass corrosion. *Nature materials*, **2015**, *14.3* 307-311.



609 Holzer, L., Indutnyi, F., Gasser, Ph., Münch, B., Wegmann, M., Three-dimensional analysis  
610 of porous BaTiO<sub>3</sub> ceramics using FIB nanotomography, *J. Microsc.* **2004**, 216, 84–95.  
611 DOI: 10.1111/j.0022-2720.2004.01397.x

612 International Atomic Energy Agency (IAEA). *The environmental behaviour of radium:*  
613 *revised edition*; IAEA: Vienna, Austria, 2014.

614 Jamieson, J. W., Hannington, M. D., Tivey, M. K., Hansteen, T., Williamson, N. M. B.,  
615 Stewart, M., Fietzke, J., Butterfield, D., Frische, M., Allen, L. Precipitation and growth  
616 of barite within hydrothermal vent deposits from the Endeavour Segment, Juan de Fuca  
617 Ridge. *Geochim. Cosmochim. Acta* **2016**, 173, 64–85. DOI: 10.1016/j.gca.2015.10.021

618 Klinkenberg, M., Brandt, F., Breuer, U., Bosbach, D. Uptake of Ra during the  
619 Recrystallization of Barite: A Microscopic and Time of Flight-Secondary Ion Mass  
620 Spectrometry Study. *Environ. Sci. Technol.* **2014**, 48, 6620–6627. DOI:  
621 10.1021/es405502e

622 Kondash, A. J., Warner, N. R., Lahav, O., Vengosh, A. Radium and barium removal through  
623 blending hydraulic fracturing fluids with acid mine drainage. *Environ. Sci. Technol.*  
624 **2014**, 48, 1334–1342. DOI: 10.1021/es403852h

625 Kovács, A., Schierholz, R., Tillmann, K. FEI Titan G2 80-200 CREWLEY. *J. large-scale*  
626 *Res. Facil. JLSRF* **2016**, 2, A43.

627 Kruth, M., Meertens, D., Tillmann, K. FEI Helios NanoLab 460F1 FIB-SEM. *J. large-scale*  
628 *Res. Facil. JLSRF* **2016**, 2, A59.

629 Luysberg, M.; Heggen, M.; Tillmann, K. FEI Tecnai G2 F20. *J. large-scale Res. Facil.*  
630 *JLSRF* **2016**, 2, A77.

631 Meertens, D., Kruth, M., Tillmann, K. FEI Helios NanoLab 400S FIB-SEM. *J. large-scale*  
632 *Res. Facil. JLSRF* **2016**, 2, A60.

633 Pollok, K., Putnis, C. V., Putnis, A.. Mineral replacement reactions in solid solution-aqueous  
634 solution systems: Volume changes, reactions paths and end-points using the example of  
635 model salt systems. *A.J.S.*, **2011**, 311(3), 211-236. DOI: 10.2475/03.2011.02

636 Putnis, A., Austrheim, A. Mechanisms of metasomatism and metamorphism on the local  
637 mineral scale: The role of dissolution-precipitation during mineral re-equilibration.  
638 *Metasomatism and the Chemical Transformation of Rock*. Springer Berlin Heidelberg,  
639 **2013**. 141-170. DOI: 10.1007/978-3-642-28394-9\_5

640 Putnis, C. V., Geisler, T., Schmid-Beurmann, P., Stephan, T., & Giampaolo, C. An  
641 experimental study of the replacement of leucite by analcime. *Amer. Miner.*, **2007**.  
642 92(1), 19-26. DOI: 10.2138/am.2007.2249

643 Putnis, A., and Putnis, C. V., The mechanism of reequilibration of solids in the presence of a  
644 fluid phase: *Journal of Solid State Chemistry*, **2007**, 180, 5, 1783-1786. DOI:  
645 [10.1016/j.jssc.2007.03.023](https://doi.org/10.1016/j.jssc.2007.03.023)

646 Prieto, M., Heberling, F., Rodríguez-Galán, R. M., Brandt, F. Crystallization behavior of  
647 solid solutions from aqueous solutions: An environmental perspective. *Prog. Cryst.*  
648 *Growth Charact. Mater.* **2016**, 62, 29–68. DOI: [10.1016/j.pcrysgrow.2016.05.001](https://doi.org/10.1016/j.pcrysgrow.2016.05.001)

649 Qian, G., Brugger, J., Skinner, W. M., Chen, G., Pring, A.. An experimental study of the  
650 mechanism of the replacement of magnetite by pyrite up to 300 C. *Geochim.*  
651 *Cosmochim. Acta*, **2010**, 74(19), 5610-5630. DOI: 10.1016/j.gca.2010.06.035

652 Rosenberg, Y. O., Metz, V., Ganor, J. Co-precipitation of radium in high ionic strength  
653 systems: 1. Thermodynamic properties of the Na-Ra-Cl-SO<sub>4</sub>-H<sub>2</sub>O system - Estimating

654 Pitzer parameters for  $\text{RaCl}_2$ . *Geochim. Cosmochim. Acta* **2011a**, 75, 5389–5402. DOI:  
655 [10.1016/j.gca.2011.06.042](https://doi.org/10.1016/j.gca.2011.06.042)

656 Rosenberg, Y. O., Metz, V., Oren, Y., Volkman, Y., Ganor, J. Co-precipitation of radium in  
657 high ionic strength systems: 2. Kinetic and ionic strength effects. *Geochim.*  
658 *Cosmochim. Acta* **2011b**, 75, 5403–5422. DOI: [10.1016/j.gca.2011.07.013](https://doi.org/10.1016/j.gca.2011.07.013)

659 Rosenberg, Y. O., Sadeh, Y., Metz, V., Pina, C. M., Ganor, J. Nucleation and growth kinetics  
660 of  $\text{Ra}_x\text{Ba}_{1-x}\text{SO}_4$  solid solution in NaCl aqueous solutions. *Geochim. Cosmochim. Acta*  
661 **2014**, 125, 290–307. DOI: [10.1016/j.gca.2013.09.041](https://doi.org/10.1016/j.gca.2013.09.041)

662 Ruiz-Agudo, E., Putnis, C.V., Putnis, A., Coupled dissolution and precipitation at mineral–  
663 fluid interfaces. *Chem. Geol.* **2014**, 383, 132-146. DOI:  
664 [10.1016/j.chemgeo.2014.06.007](https://doi.org/10.1016/j.chemgeo.2014.06.007)

665 Stack, A.G. Next generation models of mineral growth and carbonate mineral growth and  
666 dissolution. *Ghg*, **2014**, 4 (3), 278–288. DOI: [10.1002/ghg.1400](https://doi.org/10.1002/ghg.1400)

667 Stack, A. G. Precipitation in pores: A geochemical frontier. *Rev. Mineral Geochem.*, **2015**,  
668 80, p. 165-190. DOI: [10.2138/rmg.2015.80.05](https://doi.org/10.2138/rmg.2015.80.05)

669 Stoica, L., Filip, D., Filip, G., Razvan, A., Radulescu, R. Removal of  $^{226}\text{Ra}(\text{II})$  from uranium  
670 mining and processing effluents. *J. Radioanal. Nucl. Chem.* **1998**, 229, 139–142. DOI:  
671 [10.1007/BF02389462](https://doi.org/10.1007/BF02389462)

672 Thoenen, T., Hummerl, W., Berner, U., Curti, E., The PSI/Nagra Chemical Thermodynamic  
673 Database 12/07. **2014**. Nagra Working Report NAB, 14-49.

674 Torapava, N., Ramebäck, H., Curti, E., Lagerkvist, P., Ekberg, C. Recrystallization of  $^{223}\text{Ra}$   
675 with barium sulfate. *J. Radioanal. Nucl. Chem.* **2014**, *301*, 545–553. DOI:  
676 10.1007/s10967-014-3170-6

677 Varley, A., Tyler, A., Smith, L., Dale, P., Davies, M. Mapping the spatial distribution and  
678 activity of  $^{226}\text{Ra}$  at legacy sites through Machine Learning interpretation of gamma-ray  
679 spectrometry data. *Sci. Total Environ.* **2016**, *545–546*, 654–661. DOI:  
680 [10.1016/j.scitotenv.2015.10.112](https://doi.org/10.1016/j.scitotenv.2015.10.112)

681 Vinograd, V. L., Brandt, F., Rozov, K., Klinkenberg, M., Refson, K., Winkler, B., Bosbach,  
682 D. Solid–aqueous equilibrium in the  $\text{BaSO}_4\text{–RaSO}_4\text{–H}_2\text{O}$  system: First-principles  
683 calculations and a thermodynamic assessment. *Geochim. Cosmochim. Acta* **2013**, *122*,  
684 398–417. DOI: [10.1016/j.gca.2013.08.028](https://doi.org/10.1016/j.gca.2013.08.028)

685 Weber, J., Barthel, J., Brandt, F., Klinkenberg, M., Breuer, U., Kruth, M., Bosbach, D. Nano-  
686 structural features of barite crystals observed by electron microscopy and atom probe  
687 tomography. *Chem. Geol.* **2016**, *424*, 51–59. DOI: [10.1016/j.chemgeo.2016.01.018](https://doi.org/10.1016/j.chemgeo.2016.01.018)

688 Weigl, F., Trinkl, A., Crystal chemistry of radium, II, radium salts of the type  $\text{RaXO}_4$ , X=S,  
689 Se, Cr, Mo, W, *Radiochim. Acta*, **1968**, *9*: 140-4.

690 Zhang, T., Gregory, K., Hammack, R. W., Vidic, R. D. Co-precipitation of Radium with  
691 Barium and Strontium Sulfate and Its Impact on the Fate of Radium during Treatment  
692 of Produced Water from Unconventional Gas Extraction. *Environ. Sci. Technol.* **2014**,  
693 *48*, 4596–4603. DOI: 10.1021/es405168b

694 Zhang, X., He, Y., Sushko, M.L., Liu, J., Luo, L., De Yoreo, J.J., Mao, S.X., Wang, C.,  
695 Rosso, K. Direction-specific van der Waals attraction between rutile  $\text{TiO}_2$  nanocrystals.  
696 *Science*. **2017**, *356*, 6336, 434-437. DOI: 10.1126/science.aah6902

- 697 Zhang, Y., *Geochemical kinetics*, Princeton University Press, **2008**,.
- 698 Zhang, Y., Ni, H., Chen, Y., Diffusion data in silicate melts: *Reviews in Mineralogy and*  
699 *Geochemistry*, **2010**, v. 72, no. 1, p. 311-408.
- 700